Review of Scientific Instruments

Performance and simulated moment uncertainties of an ion spectrometer with asymmetric 2π field of view for ion measurements in space

Cite as: Rev. Sci. Instrum. **92**, 024501 (2021); https://doi.org/10.1063/5.0028866
Submitted: 07 September 2020 . Accepted: 22 January 2021 . Published Online: 18 February 2021

B. Su, L. G. Kong, A. B. Zhang, B. Klecker, C. P. Escoubet, D. O. Kataria, and L. Dai

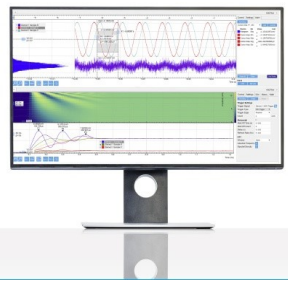

AIP Publishing

Review of Scientific Instruments ARTICLE scitation.org/journal/rsi

Performance and simulated moment uncertainties of an ion spectrometer with asymmetric 2π field of view for ion measurements in space

Cite as: Rev. Sci. Instrum. 92, 024501 (2021); doi: 10.1063/5.0028866
Submitted: 7 September 2020 • Accepted: 22 January 2021 •
Published Online: 18 February 2021

B. Su,[1,2,3] L. G. Kong,[1,2,3,4,a)] A. B. Zhang,[1,2,3,4] B. Klecker,[5] C. P. Escoubet,[6] D. O. Kataria,[7] and L. Dai[1,8]

AFFILIATIONS

[1]National Space Science Center, Chinese Academy of Sciences, Beijing 100190, China
[2]Beijing Key Laboratory of Space Environment Exploration, Beijing 100190, China
[3]Key Laboratory of Environmental Space Situation Awareness Technology, Chinese Academy of Sciences, Beijing 100190, China
[4]School of Astronomy and Space Science, University of Chinese Academy of Sciences, Beijing 100049, China
[5]Max-Planck-Institut für extraterrestrische Physik, Garching 85748, Germany
[6]European Space Research and Technology Center, European Space Agency, Noordwijk 2201AZ, The Netherlands
[7]Mullard Space Science Laboratory, University College London, Holmbury St. Mary, Surrey RH5 6NT, United Kingdom
[8]State Key Laboratory of Space Weather, National Space Science Center, Chinese Academy of Sciences, Beijing 100190, China

[a)]**Author to whom correspondence should be addressed:** klg@nssc.ac.cn

ABSTRACT

Space plasma instruments provide 3D particle velocity distribution functions. Because of telemetry limitations, these cannot be transmitted in high time resolution and the plasma needs to be characterized by moments of the velocity distribution function. These moment uncertainties have vital effects on the reliability and accuracy of onboard plasma moments. We assess the measurement accuracy for magnetosheath and solar wind ions using an ion spectrometer with an asymmetric field of view designed for the all-sky measurement of low-energy ions in the magnetosheath and solar wind. We focus on moment uncertainties for the ideal spectrometer, not considering the background counts, which may have considerable effects on the uncertainties in real life. To obtain number density, bulk velocity, and temperature, different orders of moments are integrated assuming a Maxwellian velocity distribution. Based on the design specifications, we use simulations to estimate systematic and random errors for typical plasma conditions. We find that the spectrometer resolution is adequate for determining the density of solar wind (~7% error) and magnetosheath ions (~4% error). The resolution is also adequate for determining the temperature of solar wind (~10% error) and magnetosheath ions (~2% error). For high speed flows with a bulk velocity of 750 km/s and a temperature of 20 eV, the maximum density and temperature errors become 9% and 7%, respectively. The bulk velocity errors are less than 2% for all cases. The contributions of heavy ions to the systematic errors are less than 5% for magnetosheath ions and less than 8% for solar wind ions.

I. INTRODUCTION

The velocity distribution functions of space plasmas have been measured by many different instruments and techniques since the 1960s.[1–3] Detailed experimental methods for particle distribution function analysis and space plasma parameter measurements were described first by Vasyliunas.[4] Many theoretical and experimental studies used moments of the distribution function to study the plasma parameters including number densities, bulk velocities, and temperatures. Later, in the 1980s, the accuracy of

computed moments was assessed, for example, for the AMPTE-IRM[5] 3D plasma instrument, including the effects of energy range, energy and angular resolutions, and sensitivity. On-board data analysis techniques were described for fast moment calculations with the AMPTE-IRM 3D plasma instrument and for the on-board determination of pitch angle distributions with the Giotto Rème plasma analyzer.[6]

On-board moment calculations are essential for space plasma instruments because the telemetry rate usually does not allow to transmit the full 3D plasma distributions with high time resolution and the moments are used to characterize and understand processes that occur in the solar-terrestrial system. The accuracy of moments is seriously influenced and compromised by measurement uncertainties that generally include systematic errors and random errors due to limited counting statistics. Space plasma moment calculation and error assessments have been carried out for a long time, and most of them focus on systematic errors that arise from uncertainties in instrument response, insufficient resolutions, limited energy ranges, and spacecraft charging effects.[7–10] Furthermore, space plasma instruments that detect individual particles are susceptible to statistical uncertainties due to a finite number of counted particles. The effect of counting statistics on the accuracy of results was surveyed for space plasma measurements with the AMPTE-UKS ion instrument.[11] The measurement accuracy was estimated for the CLUSTER CIS instrument, taking into account the effects of both particle counts and instrument characteristics.[12] A new analytical method was proposed in Ref. 13 to estimate uncertainties due to random counting errors in an arbitrary differentiable function of moments.

With the requirements of faster plasma measurements and large field of view (FOV) on three-axis stabilized spacecraft, instruments with wider FOVs are urgently needed. Symmetric deflectors are supplemented to expand the original elevation range up to a maximum value of ±45° by plasma instruments such as *DS-1*/PEPE,[14] *Juno*/JADE,[15] *MAVEN*/STATIC,[16] *MAVEN*/SWEA,[17] *MAVEN*/SWIA,[18] and *PSP*/SWEAP.[19] To satisfy the all-sky observation requirement, asymmetric deflector configurations have been developed to obtain elevation angles between 0° and 90°.[20,21] Many studies have been carried out aiming at the moment calculation and error analysis for symmetric FOV instruments. However, similar studies toward the assessment of moment errors for asymmetric FOV instruments do not appear to have been carried out. With a different FOV configuration, instrument responses such as azimuthal expansion, elevation resolution variation, and ion counts variability within the asymmetric FOV may be quite different from those of instruments with symmetric FOVs.[22]

Solar wind and magnetosheath ions represent two typical ion populations in space, which are quite different in their characteristics such as temperatures, velocities, and densities and have been investigated by missions including *PSP*,[19] *Cluster* II,[23] *STEREO*,[24] and *MMS*.[25] To detect the two different types of ions populations, an ion spectrometer with a high resolution ion optical system and wide FOV is required.

In this paper, we present the main technical parameters of an ion spectrometer with a wide asymmetric FOV and high energy and angular resolution for low-energy ion detection in the solar wind and magnetosheath. We calculate moments such as number density, bulk velocity, and temperature of ions based on the asymmetric FOV design and assess the moment uncertainties for the measurement of ion distributions. To acquire a complete three-dimensional ion velocity distribution, the FOV scanning deflectors of the spectrometer have a 90° coverage of elevation and uniformity in the elevation resolution, energy response, and sensitivity throughout the elevation range. Through the combination of an electrical FOV scan and 360° azimuthal position detection, the cylindrically symmetric spectrometer achieves a 2π hemispherical FOV. To achieve the all-sky measurement of the magnetosheath and solar wind ions, we assume that two spectrometers are mounted on the satellite platform pointing in opposite directions.

The ion spectrometer can determine moments of ions from the magnetosheath and solar wind with bulk velocities from 100 km/s to 2000 km/s. In this paper, we present simulation results of moment errors based on the technical parameters of the spectrometer. We use drifting Maxwellians for the magnetosheath and solar wind ion velocity distribution functions as input and calculate the output moments by integrating the distribution functions in velocity phase space. The root mean square deviation (RMSD) between the outputs and inputs mainly arises from two kinds of errors: systematic errors caused by limited energy and angular resolutions and random errors caused by the particle counting statistics. The uncertainties of the three parameters density, velocity, and temperature characterize the measurement uncertainties of the spectrometer. As spacecraft charging effects are closely related to the satellite structure and surface properties, the contribution of spacecraft charging effects on the uncertainties is not included here and will be discussed in the future.

II. DESCRIPTION OF THE SPECTROMETER

A. High resolution ion optical system

Ions from the Earth's magnetosheath and solar wind are detected by the high resolution ion spectrometer. The ion optical system has five main components illustrated in Fig. 1(a): (1) a field of view deflector system, (2) a variable geometric factor system, (3) a spherical electrostatic analyzer, (4) a microchannel plate (MCP) detector, and (5) a discrete anode position-sensitive readout. Figure 1(b) shows an example of electric field equipotential lines of the spectrometer with the electrostatic analyzer inner plate biased to −178 V, the upper deflector to −200 V, the MCP to −2000 V, and other electrodes grounded.

The wide-FOV analyzer simultaneously detects the energies and directions of incident ions over a 2π sr (steradian) FOV. The scanning voltages biased on upper and lower FOV deflectors enable the 90° coverage of elevation angle. Incident ions from directions covering 2π sr are deflected into the collimator with an elevation of 30°. The variable geometric factor system contains a top cap electrode that adjusts the geometric factor by two orders of magnitude via a top cap voltage.[26,27] The energy of the ions is selected by a voltage scan on the spherical analyzer with a resolution of ~10%. Ions exiting the analyzer will hit the MCP detector and produce charge pulse signals. After being amplified by the MCP and collected by discrete anodes, the pulse signals are accumulated and analyzed by the data processing unit for scientific applications.

Figure 2 shows a general view of ion focusing effects and anode division. Ions that enter the ion optical system on parallel trajectories

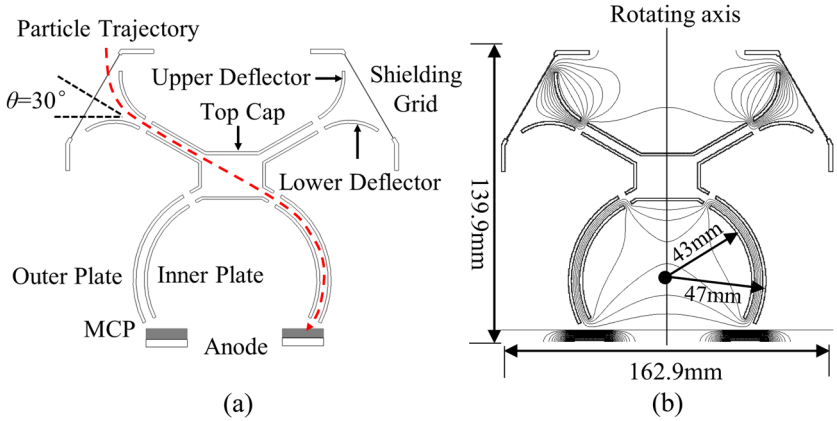

FIG. 1. (a) Simplified schematic diagram of the ion optics of the spectrometer. The ion optics consist of a grounded shielding grid, asymmetric FOV scanning deflectors, a geometric factor adjusting channel (top cap), a spherical electrostatic analyzer (inner and outer plates), the MCP, and an anode. The red dashed line shows a typical ion trajectory through all components of the spectrometer. (b) Example of electric field equipotential lines of the spectrometer with the electrostatic analyzer inner plate biased to −178 V, the upper deflector to −200 V, the MCP to −2000 V, and other electrodes grounded. Mechanical dimensions of the spectrometer are also shown with a size of 162.9 × 162.9 × 139.9 mm^3, an inner electrostatic analyzer radius of 43 mm, and an analyzer gap of 4 mm.

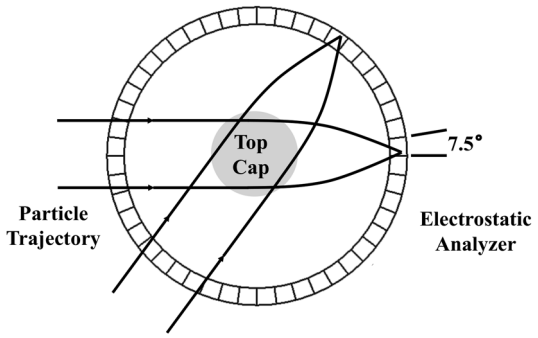

FIG. 2. Discrete anodes and ions focusing characteristics. Ions passing through all elements are focused at the exit of the electrostatic analyzer and hit the MCP. The 360° azimuth FOV is covered by 48 anodes, each providing a resolution of 7.5°.

and pass through the elements of the ion optical system are focused on the exit of the electrostatic analyzer and finally hit the MCP detector. The incident azimuth angle is determined by the ion position on the MCP. The anode is divided into 48 sectors, each providing an azimuth range of 7.5°.

B. Performance of the spectrometer

The plasma ion spectrometer measures the 3D velocity distribution function of ions in the energy range of 50 eV–20 keV in 62 logarithmically spaced energy steps. The high-resolution and wide-FOV ion optical system enables an energy resolution of 10% and a 2π sr FOV. The FOV deflectors have 16 scanning steps between 0° and 90°. Figure 3 shows examples of ion trajectories at three central incident elevations of about 0°, 30°, and 90°. Figure 4(a) illustrates the elevation response to the deflector factor *S*, which is defined as $S = (V_{up} - V_{low})/(E/q)$. Different elevation resolutions such as 5.6° and 11.25° can be reached via binning of elevation channels. Ions are deflected by the FOV deflecting voltages, guided by the collimator, selected by the electrostatic analyzer voltage, and finally captured by the MCP at the exit of the analyzer. The time resolution is defined by the energy and elevation step lengths of 0.002 s. The time resolutions for magnetosheath and solar wind ion measurements are 1.0 s and 2.0 s, respectively.

With the deflectors and the cylindrically symmetric structure, the spectrometer has a field of view of 360° by 90°, and two spectrometers pointing in opposite directions could provide a 4π sr FOV coverage of ions.

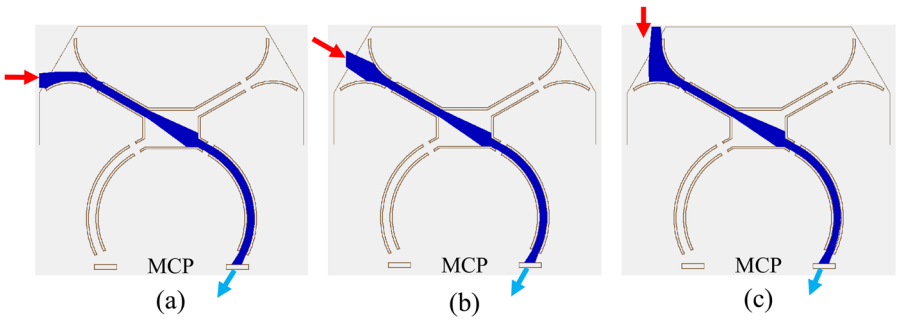

FIG. 3. Three examples of ion trajectories at different incident elevations between 0° and 90°. The central incident elevation angles are (a) 0°, (b) 30°, and (c) 90°. The central incident directions of ions are indicated by three red arrows and the exit directions by three blue arrows.

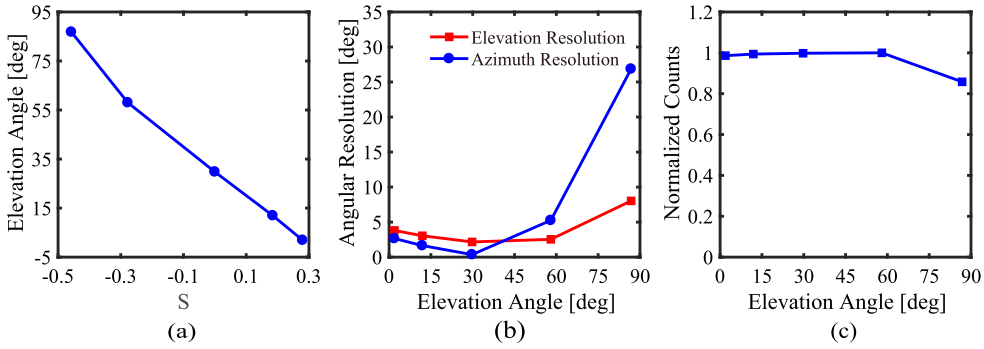

FIG. 4. (a) Elevation response to the deflector factor S, where S = (V_{up} − V_{low})/(E/q). (b) Responses of elevation resolution and azimuth resolution to the elevation angle. (c) Variation of normalized ion counts with the elevation angle.

TABLE I. Main simulated specifications of the ion spectrometer.

Parameters	Value or range
Particles detected	Low energy ions in the magnetosheath and solar wind
Energy range (keV)	0.05–20
Energy resolution	10% for 3D velocity distribution function
Field of view	2π sr (hemispherical FOV)
Elevation range (°)	0–90
Azimuth range (°)	0–360
Elevation resolution (°)	5.6, 11.25
Azimuth resolution (°)	7.5, 15.0, 22.5, 30.0
Time resolution for a full 3D scan (s)	Magnetosheath: 1.0; solar wind: 2.0
Geometric factor (cm^2 sr eV/eV)	2×10^{-4}–2×10^{-6} (per 7.5° azimuthal pixel)

The 360° azimuth FOV is covered by 48 anodes, each providing a resolution of 7.5°. Different azimuth resolutions such as 7.5°, 15°, 22.5°, and 30° are reached via anode binning. Due to different scanning steps, the spectrometer can be set to different modes to meet the detection needs of different space plasma regions. The variable geometric factor system adopts a top cap sweeping voltage to adjust the geometric factor between 2×10^{-4} cm^2 sr eV/eV and 2×10^{-6} cm^2 sr eV/eV. The main simulated specifications of the spectrometer used in this paper by SIMION software (http://www.simion.com) are summarized in Table I.

Space plasma instruments with asymmetric FOVs usually have wider azimuth responses when the incident elevation angle approaches 90°. In the extreme case of an elevation of 90°, the azimuthal position detection ranges throughout 360°.[28] In addition, when parallel ions reach the deflectors, the counts could decrease by over 50% at the elevation of 0°.[22] Figures 4(b) and 4(c) illustrate angular resolutions and ion counts response with the elevation angle. The elevation and azimuth resolutions show a smooth variation over the elevation range of 0°–90°. The ion spectrometer's asymmetric FOV utilizes a deflector inclination of 30° [θ in Fig. 1(a)], rather than 45° used in previous studies,[20,21] to narrow down the azimuth response at the elevation of 90° by about 50% (from 52° in previous studies to 26° in this paper) and enable the consistency of counts above 85% through the elevation range.

III. THEOREMS FOR MOMENT CALCULATION AND ERROR ANALYSIS

A. Definition of space plasma moments

The moment M_n of the velocity distribution function, $f(\mathbf{v})$, of a particular particle species is defined as

$$M_n = \int f(\mathbf{v})\mathbf{v}^n d\mathbf{v}, \tag{1}$$

where $\mathbf{v}^n$ is an n-fold dyadic product and d$\mathbf{v}$ is the volume element in velocity space.

The commonly used moments, number density N, bulk velocity vector $\mathbf{V}$, and pressure tensor $\mathbf{P}$ are defined as follows:[4,9]

$$N = \int f(\mathbf{v})d\mathbf{v}, \tag{2a}$$

$$\mathbf{V} = \frac{1}{N}\int f(\mathbf{v})\mathbf{v}d\mathbf{v}, \tag{2b}$$

$$\mathbf{P} = m\int f(\mathbf{v})(\mathbf{v}-\mathbf{V})(\mathbf{v}-\mathbf{V})d\mathbf{v}. \tag{2c}$$

Using the definition $\mathbf{P} = N \cdot k_B \cdot \mathbf{T}$, one can convert the pressure tensor into a temperature tensor. In this paper, we focus on the number density, bulk velocity, and scalar temperature of solar

wind and magnetosheath ions. Non-diagonal components in the pressure tensor or higher moments are not calculated and discussed. Scalar pressures and temperatures can be obtained from the traces of the associated tensors: $p = \mathrm{Tr}(\mathbf{P})/3$ and $T = \mathrm{Tr}(\mathbf{T})/3 = p/(N \cdot k_B)$. In these formulas, m is the particle mass and k_B is the Boltzmann constant.

B. Analysis methods of measurement errors

Scientific data from space plasma instruments are usually in the form of an array of phase space density f_{ijk} centered on velocities (α_i, β_j, v_k), where α_i and β_j are discrete azimuth and elevation angles, respectively. Each array is the average over acceptance volume of the spectrometer. In order to calculate moments of the discrete distribution, the integral formula of moments need to be converted to summation forms via the following expression:

$$d\mathbf{v} = v^2 \sin\beta d\alpha d\beta dv. \tag{3}$$

A simulation method is presented to analyze systematic errors due to the characteristics of the designed spectrometer and random errors due to particle counting statistics. Moments are calculated using the discrete summation formulas. First, assuming a Maxwellian velocity distribution, input parameters including number density, bulk velocity, and temperature are selected to calculate a count matrix C_{ijk} and phase space density f_{ijk} in a single integrating element. We use an accumulation time of 0.002 s for each electrostatic analyzer and a deflection voltage step for the calculation of C_{ijk}. Second, a random number of counts obeying Poisson distribution are generated, and output values of moments are obtained by integrating these random count matrices. Finally, different kinds of errors are extracted by comparing the input and output moments. The same method is applied to obtain measurement errors for a range of the three input parameters: number density, bulk velocity, and temperature. An ideal spectrometer with equal sensitivity and no noise is assumed for the simulation. The background subtraction, which may have a considerable effect on the moments and uncertainties, is not taken into consideration for the ideal spectrometer in our paper and should be analyzed carefully during future in-flight calibrations. Detailed steps for moment calculation and error analysis are shown in Fig. 5.

To calculate moments from count matrices, integral formulas introduced above are converted to discrete forms as follows:

$$N = \sum_i \sum_j \sum_k \frac{C_{ijk}'}{t_{acc} \cdot v_k^4 \cdot G_{ijk}} \cdot v_k^2 \cdot sin\beta_j \cdot \Delta\alpha_i \cdot \Delta\beta_j \cdot \Delta v_k, \tag{4}$$

$$V_x = \frac{1}{N} \sum_i \sum_j \sum_k \frac{C_{ijk}'}{t_{acc} \cdot v_k^4 \cdot G_{ijk}} \cdot v_k^3 \cdot cos\alpha_i \cdot sin^2\beta_j \cdot \Delta\alpha_i \cdot \Delta\beta_j \cdot \Delta v_k, \tag{5a}$$

$$V_y = \frac{1}{N} \sum_i \sum_j \sum_k \frac{C_{ijk}'}{t_{acc} \cdot v_k^4 \cdot G_{ijk}} \cdot v_k^3 \cdot sin\alpha_i \cdot sin^2\beta_j \cdot \Delta\alpha_i \cdot \Delta\beta_j \cdot \Delta v_k, \tag{5b}$$

$$V_z = \frac{1}{N} \sum_i \sum_j \sum_k \frac{C_{ijk}'}{t_{acc} \cdot v_k^4 \cdot G_{ijk}} \cdot v_k^3 \cdot sin\beta_j \cdot cos\beta_j \cdot \Delta\alpha_i \cdot \Delta\beta_j \cdot \Delta v_k, \tag{5c}$$

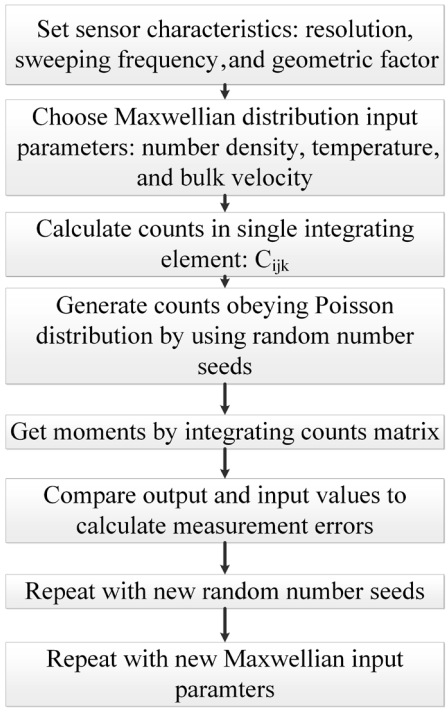

FIG. 5. Flowchart of moment calculation.

$$P_{xx} = m \cdot \sum_i \sum_j \sum_k \frac{C_{ijk}'}{t_{acc} \cdot v_k^4 \cdot G_{ijk}} \cdot v_k^4 \cdot cos^2\alpha_i \cdot sin^3\beta_j \cdot \Delta\alpha_i \cdot \Delta\beta_j \cdot \Delta v_k - m \cdot V_x^2 \cdot N, \tag{6a}$$

$$P_{yy} = m \cdot \sum_i \sum_j \sum_k \frac{C_{ijk}'}{t_{acc} \cdot v_k^4 \cdot G_{ijk}} \cdot v_k^4 \cdot sin^2\alpha_i \cdot sin^3\beta_j \cdot \Delta\alpha_i \cdot \Delta\beta_j \cdot \Delta v_k - m \cdot V_y^2 \cdot N, \tag{6b}$$

$$P_{zz} = m \cdot \sum_i \sum_j \sum_k \frac{C_{ijk}'}{t_{acc} \cdot v_k^4 \cdot G_{ijk}} \cdot v_k^4 \cdot sin\beta_j \cdot cos\beta_j^2 \cdot \Delta\alpha_i \cdot \Delta\beta_j \cdot \Delta v_k - m \cdot V_z^2 \cdot N. \tag{6c}$$

Note that the moments are calculated by using the geometric factor G_{ijk} but not including the variable geometric factor function. Combining the components of bulk velocity and pressure, the bulk velocity and temperature can be obtained by using the following relations:

$$V = \sqrt{V_x^2 + V_y^2 + V_z^2}, \tag{7a}$$

$$T = \frac{P_{xx} + P_{yy} + P_{zz}}{3 \cdot N \cdot k_B}. \tag{7b}$$

To evaluate the measurement uncertainties, we utilize RMSD by comparing all outputs to the input values, with the differences being due to the combined effect of systematic and random errors. Ions at several typical incident elevations are chosen to analyze

the errors caused by the spectrometer characteristics and counting statistics. The spectrometer is specifically designed for measurements in the magnetosheath and solar wind (including high speed flows). We present, therefore, simulation results of moment uncertainties in these environments. In low-density (low-count) plasma, random errors can be one of the dominant sources of moment uncertainties. Therefore, we display the random errors to help estimate the spectrometer performance in some low-flux conditions.

Here, we define the three errors mentioned above. For each input moment X_0, total M count matrices were generated, and the moment was calculated M times (M is set 300 in this paper). The RMSD of a moment is defined as the root mean square deviation percentage between all outputs and the input value,

$$\delta_{\mathrm{RMSD}} = \frac{\sqrt{\frac{1}{M-1}\sum_{i=1}^{M}(X_i - X_0)^2}}{X_0}. \tag{8}$$

The systematic error of a moment is defined to assess the mean deviation between the outputs and the input value,

$$\delta_{systematic} = \frac{\overline{X} - X_0}{X_0}. \tag{9}$$

The random error of a moment is defined as the root mean square deviation percentage between all outputs and the mean value of a specific moment,

$$\delta_{\mathrm{random}} = \frac{\sqrt{\frac{1}{M-1}\sum_{i=1}^{M}(X_i - \overline{X})^2}}{\overline{X}}, \tag{10}$$

where X_i is the output value and $\overline{X}$ is the mean value of all outputs for a specific moment.

IV. SIMULATION RESULTS

The spectrometer has different modes to fulfill different measurement requirements. Here, we consider two modes for magnetosheath and solar wind ion measurements. The magnetosheath mode scans the elevation between 0° and 90° in 8 steps, and the solar wind mode scans the same elevation range in 16 steps. Therefore, elevation resolutions for magnetosheath and solar wind ion measurements are 11.25° and 5.6°, respectively. A complete summation over the 4π sr FOV needs 47 616 count matrix elements (62 energies × 8 elevations × 2 × 48 azimuths) for the magnetosheath and 95 232 count matrix elements (62 energies × 16 elevations × 2 × 48 azimuths) for the solar wind. In Fig. 6, examples of sampling energies and elevation angles of the distribution function of ions in the magnetosheath, solar wind, and high speed flows are shown with an incident elevation angle of 0° as an example. The centered bulk velocities are 300 km/s, 400 km/s, and 750 km/s for magnetosheath ions, solar wind ions, and high speed flow ions, respectively. Energies are sampled logarithmically in the range of 50 eV–20 keV, and elevation angles are sampled linearly in the range of −90°–90°.

To illustrate the typical number of counts of ions in the accumulation time of 2 ms, we use typical values of 10 cm^{-3} (1 cm^{-3}) for the density, 500 eV (10 eV) for the temperature, and 300 km/s (400 km/s) for the velocity of magnetosheath (solar wind) ions. From the counts' distribution in Fig. 7, we can conclude that typical maximum counts in one bin for magnetosheath and solar wind ion measurements with our ion spectrometer are about 20.3 and 178.4 counts in 2 ms, respectively, for the plasma parameters shown above.

A. Magnetosheath ion measurements

Ions in the magnetosheath mainly come from the decelerated solar wind, usually with larger number densities and higher temperatures than in the solar wind. We evaluate RMSDs of the number density, the temperature, and the bulk velocity for magnetosheath densities of 0.01 cm^{-3}–100 cm^{-3}, temperatures of 10 eV–10^4 eV, a typical bulk velocity of 300 km/s, and three elevation angles (0°, 45°, and 90°). We note that typical values of number densities and temperatures for magnetosheath ions are 1 cm^{-3}–10 cm^{-3}, and 500 eV,[12,29,30] respectively.

The RMSD simulation results for magnetosheath ions are displayed in Fig. 8, and RMSD percentages are indicated in the color bar.

At the elevation of 0°, RMSDs of the number density, the temperature, and the bulk velocity decrease as the input density increases. RMSDs of the number density, the temperature, and the bulk velocity in magnetosheath are at most 4%, 2%, and 2%, respectively, when the input number density varies between

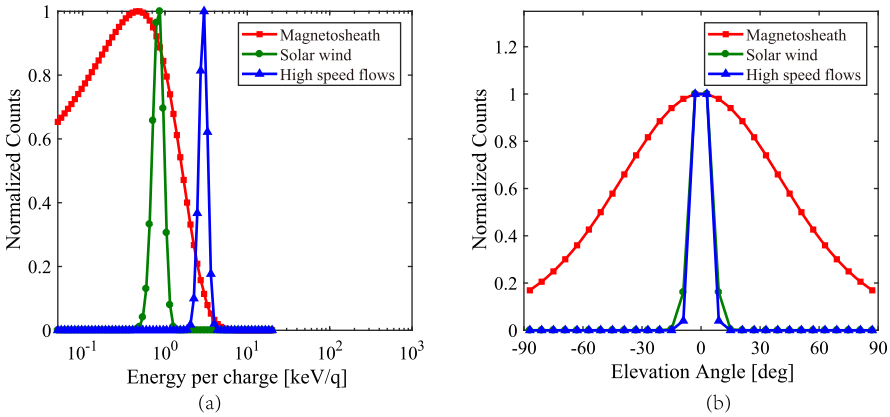

FIG. 6. Examples of (a) sampling energies and (b) elevation angles of the distribution function of ions in the magnetosheath, solar wind, and high speed flows. Each marker represents a sampling energy or elevation angle step for ions in the magnetosheath (red solid squares), solar wind (green solid dots), and high speed flows (blue solid triangles).

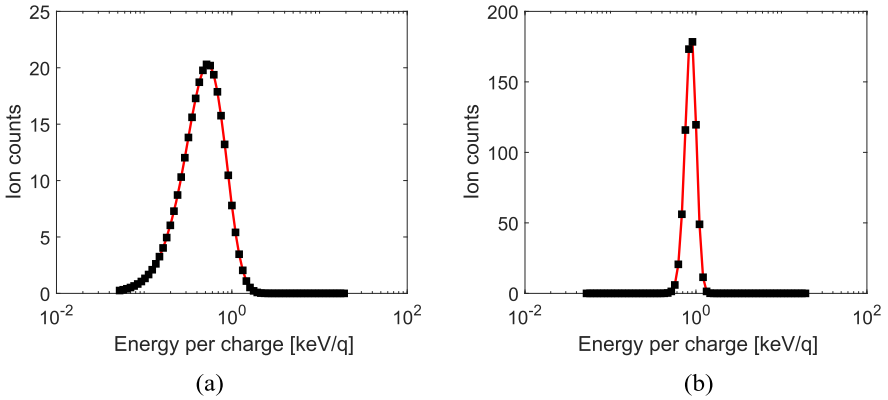

FIG. 7. Typical maximum counts for (a) magnetosheath (N = 10 cm^{-3}, V = 300 km/s, and T = 500 eV) and (b) solar wind ions (N = 1 cm^{-3}, V = 400 km/s, and T = 10 eV). The incident elevations for the two panels are selected to be 45° as an example. The counts are selected for the anode sector with maximum counts (the 0° azimuth angle).

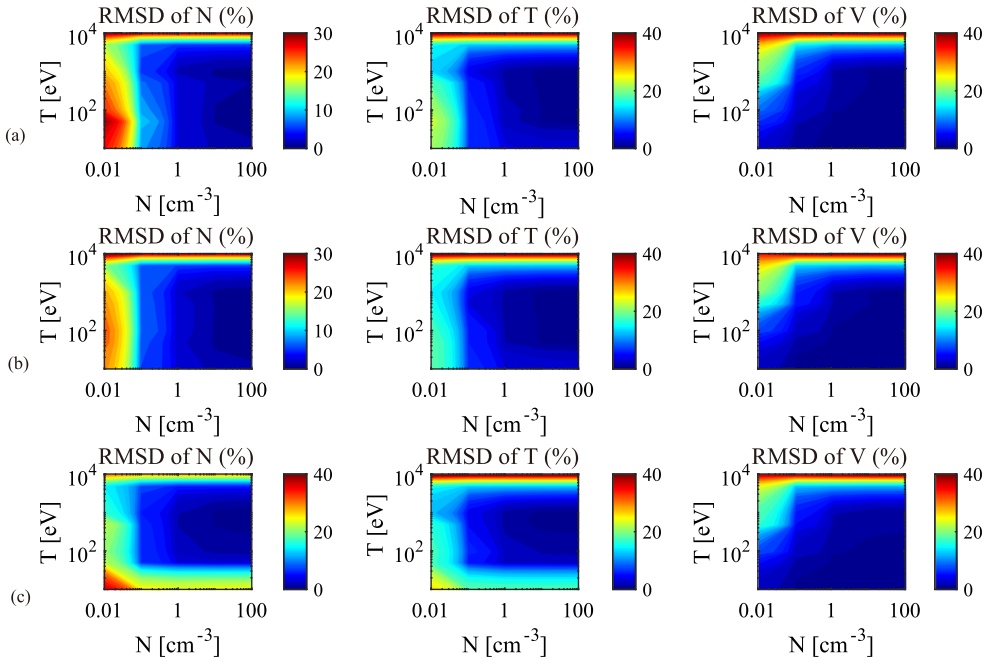

FIG. 8. Number density, temperature, and bulk velocity RMSDs of magnetosheath ions (V = 300 km/s) at (a) 0° elevation angle, (b) 45° elevation angle, and (c) 90° elevation angle.

1 cm^{-3} and 10 cm^{-3}. When the input density is larger than 10 cm^{-3}, the corresponding RMSDs will drop to 2%, 1%, and 1%, respectively.

RMSDs at the elevation of 45° are almost the same as those at the elevation of 0° because the spectrometer performance changes only slightly when the deflectors scan from 45° to 0°.

At the elevation of 90°, RMSD contour plots of the number density and the temperature become different because the azimuth response gets wider when the incident elevation approaches 90°. The azimuth response spread should be smooth and gradual. The deflectors have a spherical shape, which we found to be the best to meet the performance requirements, with an extreme azimuth resolution of better than 30° at the elevation very close to 90°. Larger errors occur at the lowest temperature of 10 eV and the highest temperature of 10^4 eV. The density RMSD in the magnetosheath is at most 2% when the input density is 1 cm^{-3}–10 cm^{-3} and the input temperature is ~500 eV. The temperature and bulk velocity RMSDs are less than 2% under the same input conditions. When the input density is larger than 10 cm^{-3}, the density and temperature RMSDs drop to less than 1%.

In order to clarify the contribution of systematic errors to the RMSD contour lines, we illustrate systematic errors at different elevation angles for magnetosheath ions determination in Fig. 9. We chose a temperature range of 10^2 eV–10^4 eV and a velocity range of 100 km/s–400 km/s to cover typical magnetosheath ion parameters. The systematic error is density independent according to the systematic error definition. At the elevation of 0°, the systematic error of density is about −1.5%, while both temperature and velocity systematic errors are about −1%. Negative errors mean that the output

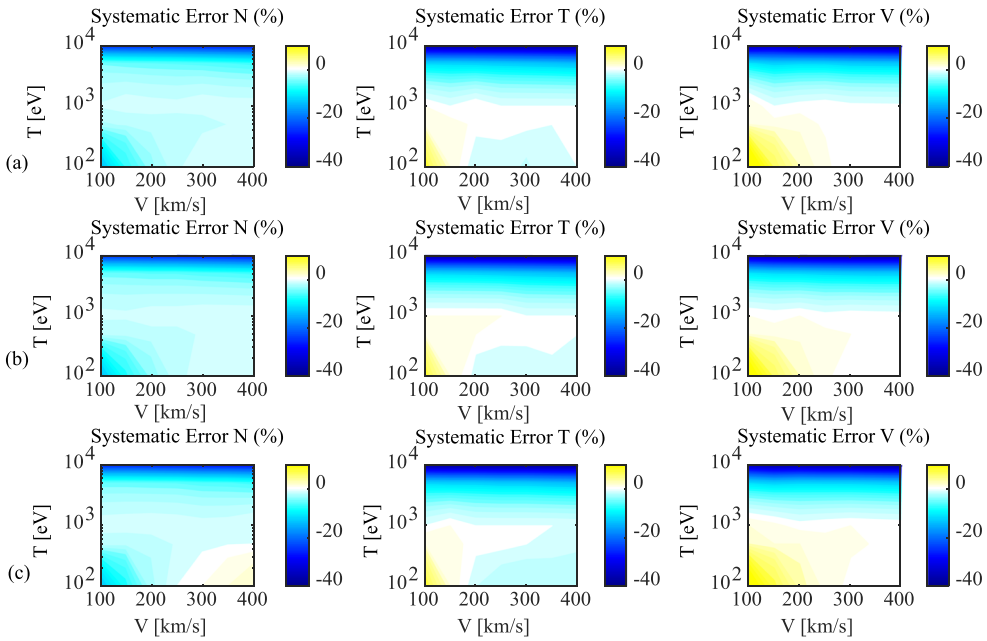

FIG. 9. Number density, temperature, and bulk velocity systematic errors of magnetosheath ions at (a) 0° elevation angle, (b) 45° elevation angle, and (c) 90° elevation angle.

value is smaller than the input value. At the elevation of 45°, the density systematic error is about −1%, while both temperature and velocity errors are less than 1%. At the elevation of 90°, systematic errors of the number density and the temperature are both about −1%, while the systematic error of the velocity is about 1%. Systematic errors and random errors determine the shape of the RMSD contour lines together.

Another simulation was run to study the effect of the increasing counts on the accuracy of the moment determination for magnetosheath ions. For this simulation, the input velocity was fixed at 300 km/s and the input temperature at 500 eV, while the density was varied from 0.01 cm^{-3} to 100 cm^{-3}. The random errors of moments are shown in Fig. 10. It is obvious that all parameters are well measured at the magnetosheath density of 1 cm^{-3}–10 cm^{-3}, with random errors less than 3% for all the three moments. Once the density reaches values above 10 cm^{-3}, all parameters are determined to better than 1%. Random errors at different incident elevations are basically the same. Random errors of moments generally scale as $1/\sqrt{N_{cts}}$, where $N_{cts} = \sum C_{ijk}$ is the total number of counts in the distribution, which has also been found in previous studies.[11,13] Random errors are only significant for low densities of <1 cm^{-3}. Errors at the lowest and highest temperature regions of the RMSDs are mainly caused by systematic errors, which usually are due to inadequate sampling, finite resolution, and uncertainties in the spectrometer response.

B. Solar wind ion measurements

Solar wind ions have lower temperatures and higher bulk velocities than ions in the magnetosheath. With a higher elevation

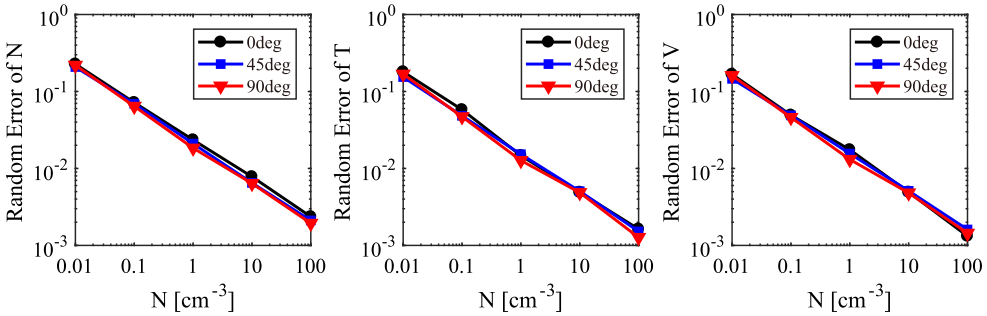

FIG. 10. Number density, temperature, and bulk velocity random errors of magnetosheath ions (V = 300 km/s and T = 500 eV) at elevation angles of 0°, 45°, and 90°.

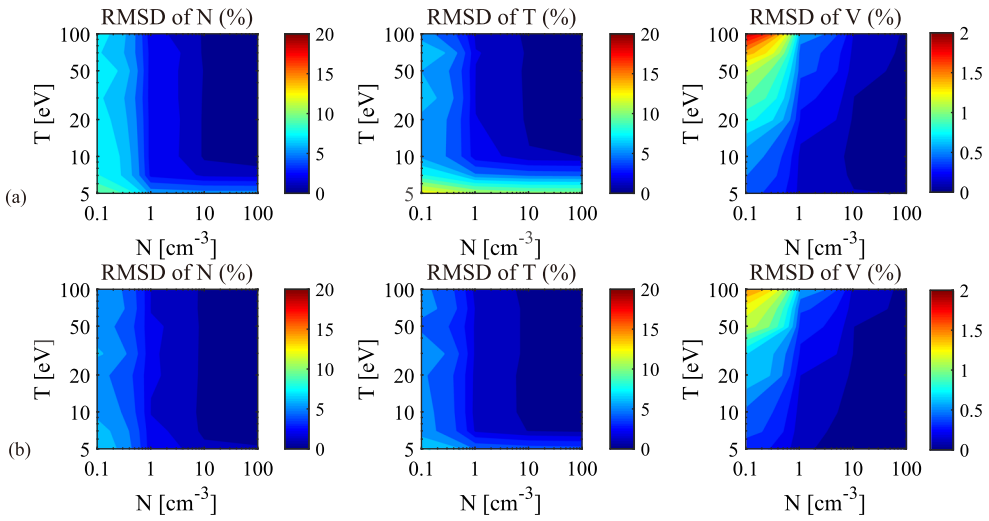

FIG. 11. Number density, temperature, and bulk velocity RMSDs of solar wind ions (V = 400 km/s) at (a) 0° elevation angle and (b) 45° elevation angle.

resolution of 5.6°, simulation results of RMSDs for solar wind ion moments are shown in Fig. 11. For this study, the bulk velocity was fixed at 400 km/s, with a density range of 0.1 cm^{-3}–100 cm^{-3} and a temperature range of 5 eV–100 eV. Since the incident solar wind ions usually have narrower distributions and are almost at the incident elevation of 0° according to the mounting of the spectrometer, with a maximum expansion of no more than 20°, only two elevation cases of 0° and 45° were taken into consideration to evaluate the measurement accuracy.

At the elevation of 0°, the density is well determined to 7% and the temperature to 10% at an extreme temperature of 5 eV. The RMSDs of the density and the temperature drop significantly to better than 3% for input temperatures of 10 eV–100 eV and number densities larger than 1 cm^{-3}. At the same temperature range, the RMSDs are less than 1%, while the input density of solar wind ions increases to 10 cm^{-3}. In the whole temperature range, the bulk velocity RMSD is less than 0.5%, and it drops further to 0.1% as the input density increases to 10 cm^{-3}.

At the elevation of 45°, the density is well determined (~3% error) for solar wind ions with a density larger than 1 cm^{-3} and the temperature higher than 5 eV. The temperature error is about 5% under the same input condition. For the input density larger than 10 cm^{-3} and the temperature higher than ~7 eV, RMSDs of both the density and the temperature are less than 1%. The bulk velocity RMSD is almost the same as in the case of the elevation of 0°.

Systematic errors for solar wind ion measurements are shown in Fig. 12. For typical solar wind ions with a velocity of 400 km/s

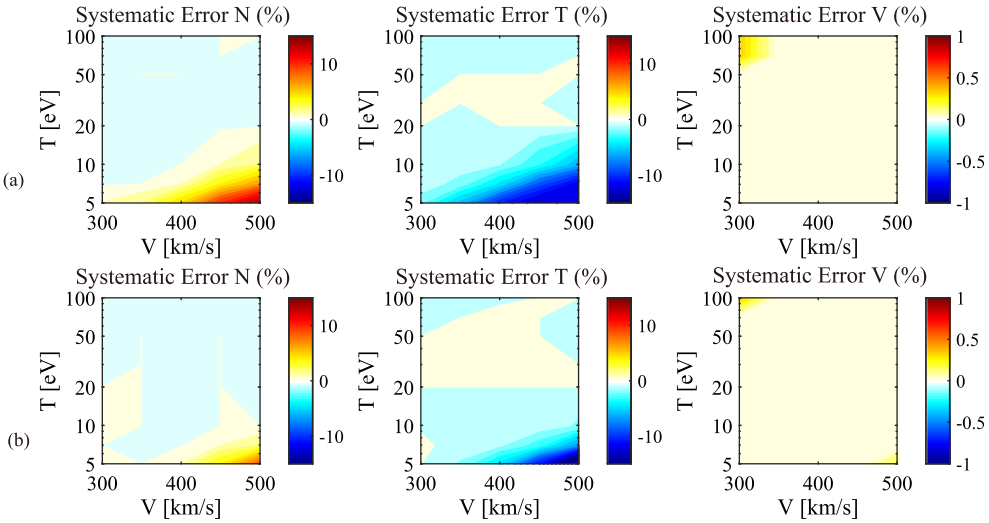

FIG. 12. Number density, temperature, and bulk velocity systematic errors of solar wind ions at (a) 0° elevation angle and (b) 45° elevation angle.

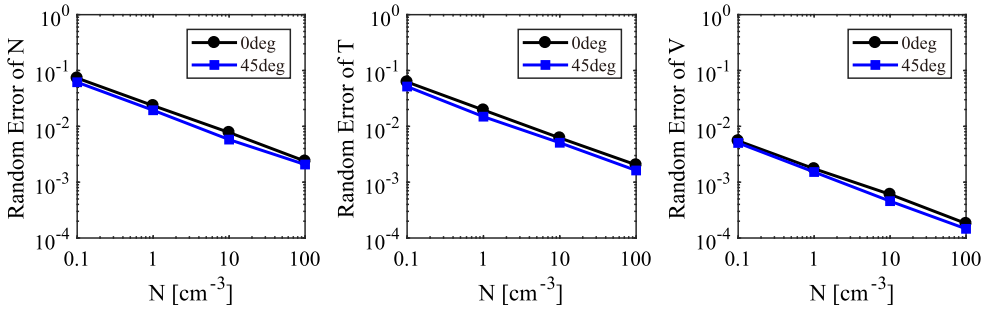

FIG. 13. Number density, temperature, and bulk velocity random errors of solar wind ions (V = 400 km/s and T = 10 eV) at elevation angles of 0° and 45°.

and a temperature of 10 eV, the density and temperature systematic errors are less than −1% and −5%, respectively, and the velocity systematic error is less than 0.1%.

Similar to the magnetosheath case, random errors of solar wind ion moments are calculated and plotted in Fig. 13. For this study, the bulk velocity was fixed at 400 km/s and the temperature at 10 eV. Random errors of the density and the temperature are about 5.1% and 4.2%, respectively, at an extreme number density of 0.2 cm^{-3} for solar wind ions.[31] Random errors of the density and the temperature are less than 3% for the input density larger than 1 cm^{-3}. They decrease to less than 1% when the input density is larger than 10 cm^{-3}. The velocity random error is less than 0.4% for solar wind density of 0.2 cm^{-3} and goes lower than 0.3% for typical solar wind density of 1 cm^{-3}. Random errors in the solar wind decrease with $1/\sqrt{N_{cts}}$ as well.

It is possible for the ion spectrometer to encounter high speed flows from coronal holes when in the solar wind. In order to evaluate the performance of the spectrometer comprehensively, the accuracy of moment measurement for high speed flows in the solar wind was also determined. The number density, temperature, and bulk velocity RMSDs for high speed flow ions at elevation angles of 0° and 45° are listed in Table II. In this simulation, the bulk velocity was fixed at 750 km/s and RMSD was evaluated for a temperature range of 15 eV–100 eV and a number density range of 0.1 cm^{-3}–100 cm^{-3}, covering typical values of the bulk velocity and the temperature of 750 km/s and 20 eV,[32] respectively.

At the incident elevation of 0°, the number density is accurate to 9% and the temperature to 7% for input densities larger than 1 cm^{-3} and input temperatures higher than 15 eV. Note that the density and temperature RMSDs for high speed flows are slightly worse than those in the solar wind of 400 km/s. When the input temperature increases to more than 20 eV, the density determined is better than 4%. In the whole temperature range, the bulk velocity RMSD is negligible (less than 0.3% error) if the input density is larger than 1 cm^{-3}.

At the incident elevation of 45°, the number density and temperature of high speed flows are accurate to 2% and 3%, respectively, for an input density of 1 cm^{-3}–10 cm^{-3} and a temperature of 20 eV–100 eV. The bulk velocity RMSD is less than 0.2%, which can be generally neglected. RMSDs for high speed flow ion moments are, to some extent, larger than those for slow solar wind and magnetosheath ions at low temperatures. This is mainly caused by the coarser samplings of the distribution function at lower temperatures and higher velocities.

In Table II, we list systematic errors for high speed flows at a velocity of 750 km/s and a temperature of 20 eV. In this case, systematic errors are obviously larger than for the magnetosheath and the slow solar wind. At the elevation of 0°, the density and temperature systematic errors increase to 3% and −7%, respectively. At the elevation of 45°, they decrease to 1% and −3%, respectively. Systematic errors of the bulk velocity at both elevations are less than 0.1%, which can generally be neglected.

TABLE II. Moment maximum uncertainties with the density larger than 1 cm^{-3} for magnetosheath and solar wind ions at different incident elevations.

Regions	Incident elevations (deg)	RMSD			Systematic error			Random error		
		N (%)	T (%)	V (%)	N (%)	T (%)	V (%)	N (%)	T (%)	V (%)
Magnetosheath	0	4	2	2	−1.5	−1	−1	2.4	1.5	1.8
	45	4	2	2	−1	0.4	1	2.1	1.5	1.6
	90	2	2	2	−1	−1	1	1.8	1.3	1.3
Solar wind	0	7	10	0.5	−1	−5	0.1	2.4	2	0.3
	45	3	5	0.5	−1	−5	0.1	1.9	1.5	0.2
Solar wind high speed flows	0	9	7	0.3	3	−7	0.1	1.6	1.7	0.1
	45	2	3	0.2	1	−3	0.1	1.3	1.1	0.1

Random errors are also shown in Table II for measurements of high speed flow ion moments. The bulk velocity was fixed at 750 km/s and the temperature at 20 eV. All parameters are well measured for high speed flows at densities more than 1 cm^{-3}, with the random error of density less than 1.6%, temperature less than 1.7%, and bulk velocity less than 0.1%. For high speed flow ion densities larger than 10 cm^{-3}, all parameters determined are better than 1%. Random errors at different incident elevations are basically the same. Random errors in the high speed flow decrease also with $1/\sqrt{N_{cts}}$.

Maximum uncertainties for ions moment determination in the magnetosheath and solar wind are listed in Table II. In summary, for all investigated cases, the current technical parameters of the spectrometer are adequate for moment determination. Measurement errors are no more than 5% for magnetosheath and no more than 10% for solar wind (including high speed flows) ion measurements. This will guarantee the excellent detection performance of the spectrometer for future space missions.

C. Systematic errors due to the presence of heavy ions

Generally, protons dominate in the solar wind and magnetosheath. But heavier ions are also present and can possibly affect the measurement accuracy for protons. The three most common ion species in the solar wind are H^+, He^{2+}, and O^{6+} and are likely to persist in the magnetosheath.[33] The number density of He^{2+} is typically a few percent of that of protons.[34]

Ions in the magnetosheath have complex and broad distributions after they penetrated the bow shock.[33,35–37] The He^{2+}/H^+ density ratio in the magnetosheath was, for example, 6.2% ± 0.6% during the magnetopause crossing recorded by MMS4 on 22 November 2015.[29] Temperatures of He^{2+} in the magnetosheath may vary over a quite broad range. It was noted in Ref. 35 that the temperature ratio was ~4 in the magnetosheath because its thermal velocities were comparable. However, the ratio varied when streams with different velocities and when coronal holes, CIRs, and ICMEs were taken into consideration.[38] To estimate the influence of the He^{2+} number density on the proton moment measurement errors by the spectrometer, a typical bulk velocity of 300 km/s and a proton temperature of 500 eV are chosen to study the broad magnetosheath ion distributions. For He^{2+}, we take a temperature of 2 keV and the same bulk velocity as that of protons. We vary the He^{2+}/H^+ number density ratio from 0% to 10%, which generally covers the range of observed ratios in the magnetosheath. The results for three incident elevation angles of 0°, 45°, and 90° are shown in Fig. 14(a). When the density ratio is zero, the errors are what we have described in Fig. 9. Maximum systematic errors of the number density, the temperature, and the bulk velocity are −2.5%, 4.9%, and 3.0% for a density ratio of 6.2%. Figures 9 and 14(a) show that the accuracy of the moments for magnetosheath ions is still better than 10%, even if a contribution of He^{2+} up to 10% is taken into account.

In Figs. 14(b) and 14(c), we show the variation of systematic errors for slow solar wind and high speed flow, respectively. Because the velocity vector of solar wind ions varies typically within ±20°, large elevation angles can be avoided by the appropriate orientation of the spectrometer relative to the sun aboard the spacecraft. For solar wind analysis, we consider two elevation angles of 0° and 45° and a number density ratio from 0% to 10%, which covers the density ratio range both in the solar wind and high speed flows. As introduced in Ref. 39 and references therein, temperature ratios of He^{2+} and H^+ at 1 AU are about 3.2 and 6.2 for the solar wind and high speed flows, respectively. When the He^{2+}/H^+ density ratio is zero, the errors are what we have shown in Fig. 12 and Table II, only taking protons into consideration. For the density ratio of 3.8% in the solar wind and 4.8% in high speed flows,[40] systematic errors of the number density and the bulk velocity have only a small variation with the density ratio. The maximum number density error is −1.2% for solar wind protons and −1.0% for protons in high speed flows. The maximum bulk velocity error is 1.3% for solar wind protons and 1.5% for protons in high speed flows. Systematic errors of the temperature would be extremely large in the solar wind and high

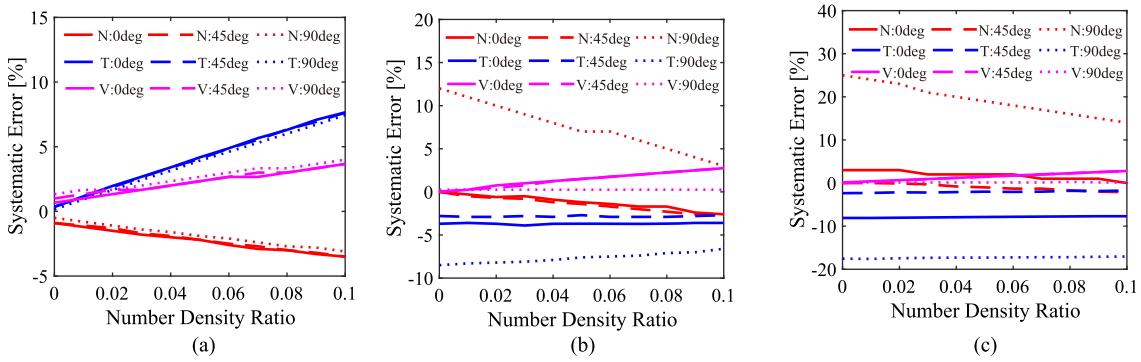

FIG. 14. (a) Systematic errors of protons in the magnetosheath affected by He^{2+} ion density at elevation angles of 0°, 45°, and 90°, with a proton bulk velocity of 300 km/s and a proton temperature of 500 eV. For He^{2+}, we assume a bulk velocity and a temperature of 300 km/s and 2 keV, respectively. (b) Systematic errors of solar wind protons affected by He^{2+} ion density at elevation angles of 0°, 45°, and 90°, with a proton bulk velocity of 400 km/s and a proton temperature of 10 eV. For He^{2+}, we assume a bulk velocity and a temperature of 400 km/s and 30 eV, respectively. (c) Systematic errors of protons in the solar wind high speed flows affected by He^{2+} ion density at elevation angles of 0°, 45°, and 90°, with a proton bulk velocity of 750 km/s and a proton temperature of 20 eV. For He^{2+}, we assume a bulk velocity and a temperature of 750 km/s and 120 eV, respectively.

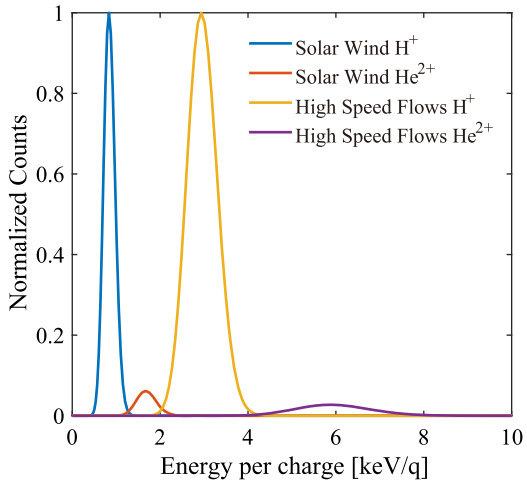

FIG. 15. Energy per charge (E/q) distributions of H^+ and He^{2+} in the solar wind and high speed flows assuming Maxwellian velocity distributions. Temperatures in the solar wind are 10 eV for H^+ and 30 eV for He^{2+}. Temperatures in high speed flows are 20 eV for H^+ and 120 eV for He^{2+}.

speed flows if heavier ions are present and not excluded from the moment calculation. However, the solar wind He^{2+} does have the same bulk velocity as protons. Therefore, in the electrostatic analyzer, the peak of He^{2+} will have about twice the energy per charge (E/q) value of that for protons. Because of the low temperature in the solar wind, the two peaks of H^+ and He^{2+} are well separated in E/q, as shown in Fig. 15. To obtain a better temperature measurement, we start in our simulation with the summation of the count matrices C_{ijk} at low energy per charge and stop before the He^{2+} peak. The temperature systematic errors are also plotted in Fig. 14(b) for the solar wind, with a maximum error of −3.7% and in Fig. 14(c) for high speed flows, with a maximum error of −7.9%. The He^{2+}/H^+ density ratio in the solar wind may vary with the solar wind speed and solar cycle, which is found to be changing periodically between 1% and 4% over Carrington rotations for different solar wind speeds over a 3-year period from 1995 through 1998[41] and not larger than 6% during four solar cycles.[42] However, the systematic errors for solar wind (including high speed flows) ion measurements at the elevations of 0° and 45° show only a small variation with the He^{2+}/H^+ density ratio.

To summarize, systematic errors due to heavy ions in the magnetosheath, the slow solar wind, and high speed flows are still better than 10%, which indicates that the spectrometer is adequate for proton moment measurements in its operating regions even if it is not equipped with a time-of-flight system that would provide separation by mass per charge.

V. CONCLUSIONS

In this paper, we have introduced the main features and performances of a new plasma spectrometer with an asymmetric FOV for the high-resolution and all-sky detection of low energy ions in near-Earth space and solar wind. In order to evaluate the accuracy of ion plasma measurements with the asymmetric FOV, we calculate moments of plasmas from different regions in near-Earth space by integrating the Maxwellian velocity distribution function over the 4π FOV and analyze the moment uncertainties. Moment calculation and error analysis are of great significance for this kind of space plasma spectrometer since a wider FOV is increasingly becoming the basic configuration for space plasma detection on non-spinning spacecraft. The spectrometer will determine the basic moments of the magnetosheath and solar wind ion distributions *in situ*, such as number density, temperature, and bulk velocity under different conditions.

The moments of ions in the magnetosheath, typical slow solar wind, and high speed flows are calculated based on the spectrometer specifications. We conclude from our simulation that the energy range and resolutions are adequate for determining the ion density in the magnetosheath (<4% error), the solar wind (<7% error), and high speed flows (<9% error). The spectrometer is also adequate for determining the ion temperature in the magnetosheath (<2% error), the solar wind (<10% error), and high speed flows (<7% error). The bulk velocity errors are less than 2% for the magnetosheath and less than 0.5% for solar wind (including high speed flows) ion measurements. While considering heavier ions' influence, the spectrometer can still perform well on determining moments of protons in all operating regions. In addition, we also estimated the influence of insufficient counts on the accuracy of the moments by calculating random errors under different input conditions. Random errors scale as $1/\sqrt{N_{cts}}$ and are less than 3% for all cases.

The simulation results for the uncertainties of the moment density, bulk velocity, and temperature show that the technical design parameters of the ion spectrometer are adequate for the high-resolution measurement of low energy ions in the magnetosheath and the solar wind. This work also lays a foundation for the future investigation of more complex distribution functions and moment error analysis over a 4π sr FOV.

ACKNOWLEDGMENTS

Our work was supported by the Strategic Priority Research Program on Space Science, the Chinese Academy of Sciences (Grant Nos. XDA1535010202 and XDA15011200). The authors would like to thank all those who assisted us in completing the spectrometer design, moment calculation, and error analysis. Calculation programs and results supporting the conclusions can be produced via methods and formulas listed in this paper. More discussions on the moment error estimation can be found in the references.

DATA AVAILABILITY

The data that support the findings of this study are available from the corresponding author upon reasonable request.

REFERENCES

[1] B. J. O'Brien, C. D. Laughlin, and D. A. Gurnett, "High-latitude geophysical studies with satellite Injun 3: 1. Description of the satellite," J. Geophys. Res. **69**, 1–12, https://doi.org/10.1029/jz069i001p00001 (1964).
[2] L. A. Frank, "A survey of electrons $E > 40$ keV beyond 5 Earth radii with Explorer 14," J. Geophys. Res. **70**, 1593–1626, https://doi.org/10.1029/jz070i007p01593 (1965).
[3] S. Singer, "The Vela satellite program for detection of high-altitude nuclear detonations," Proc. IEEE **53**, 1935–1948 (1965).

[4]V. M. Vasyliunas, "Deep space plasma measurements," in *Methods in Experimental Physics*, Plasma Physics, edited by R. H. Lovbergs (Academic, New York, 1971), Vol. 9B, pp. 49–88.
[5]G. Paschmann, I. Papamastorakis, W. Baumjohann, N. Sckopke, C. W. Carlson, B. U. Ö. Sonnerup *et al.*, "The magnetopause for large magnetic shear: AMPTE/IRM observations," J. Geophys. Res. **91**, 11099, https://doi.org/10.1029/ja091ia10p11099 (1986).
[6]D. W. Curtis, C. W. Carlson, R. P. Lin, G. Paschmann, H. Rème, and A. Cros, "On-board data analysis techniques for space plasma particle instruments," Rev. Sci. Instrum. **60**, 372 (1989).
[7]R. L. Kessel, A. D. Johnstone, C. C. Brown, and L. J. C. Woolliscroft, "A comparison of the ion density measured simultaneously by a wave and a particle instrument," J. Geophys. Res. **96**, 1833–1841, https://doi.org/10.1029/90JA01800 (1991).
[8]R. F. Pfaff, J. E. Borovsky, and D. T. Young, *Measurement Techniques in Space Plasmas: Particles*, AGU Geophysics Monograph Series Vol. 102 (AGU, Washington, DC, 1998).
[9]G. Paschmann and P. W. Daly, "Analysis methods for multispacecraft data," *ISSI Scientific Reports SR-001* (Kluwer Academic, Norwell, MA, 1998).
[10]J. A. Gilbert, D. J. Gershman, G. Gloeckler, R. A. Lundgren, T. H. Zurbuchen, T. M. Orlando *et al.*, "Invited Article: Characterization of background sources in space-based time-of-flight mass instruments," Rev. Sci. Instrum. **85**, 091301 (2014).
[11]R. L. Kessel, A. D. Johnstone, A. J. Coates, and R. A. Gowen, "Space plasma measurements with ion instruments," Rev. Sci. Instrum. **60**, 3750–3761 (1989).
[12]C. Martz, J. A. Sauvaud, and H. Rème, "Accuracy of ion distribution measurements and related parameters using the cluster CIS experiment," in *Proceedings of the International Conference Spatio-Temporal Analysis for Resolving Plasma Turbulence* (*START*) *ESA WPP*, *Aussois*, *31 January–5 February 1993* (European Space Agency, Paris, 1993), Vol. 047, pp. 229–239.
[13]D. J Gershman, J. C. Dorelli, A. F. Viñas, and C. J. Pollock, "The calculation of moment uncertainties from velocity distribution functions with random errors," J. Geophys. Res.: Space Phys. **120**, 6633–6645, https://doi.org/10.1002/2014ja020775 (2015).
[14]D. T. Young, J. E. Nordholt, J. L. Burch, D. J. McComas, R. P. Bowman, R. A. Abeyta *et al.*, "Plasma Experiment for Planetary Exploration (PEPE)," Space Sci. Rev. **129**, 327–357 (2007).
[15]D. J. McComas, N. Alexander, F. Allegrini, F. Bagenal, C. Beebe, G. Clark *et al.*, "The Jovian Auroral Distributions Experiment (JADE) on the Juno mission to Jupiter," Space Sci. Rev. **213**, 547–643 (2017).
[16]J. P. McFadden, O. Kortmann, D. Curtis, G. Dalton, G. Johnson, R. Abiad *et al.*, "MAVEN SupraThermal And Thermal Ion Composition (STATIC) instrument," Space Sci. Rev. **195**, 199–256 (2015).
[17]D. L. Mitchell, C. Mazelle, J.-A. Sauvaud, J. J. Thocaven, J. Rouzaud, A. Fedorov *et al.*, "The MAVEN Solar Wind electron Analyzer," Space Sci. Rev. **200**, 495–528 (2016).
[18]J. S. Halekas, E. R. Taylor, G. Dalton, G. Johnson, D. W. Curtis, J. P. McFadden *et al.*, "The solar Wind Ion Analyzer for MAVEN," Space Sci. Rev. **195**, 125–151 (2015).
[19]J. C. Kasper, R. Abiad, G. Austin, M. Balat-Pichelin, S. D. Bale, J. W. Belcher *et al.*, "Solar Wind Electrons Alphas and Protons (SWEAP) investigation: Design of the solar wind and coronal plasma instrument suite for solar probe plus," Space Sci. Rev. **204**, 131–186 (2016).
[20]L. Duvet, J. J. Berthelier, J. Illiano, and M. Godefroy, "A low-energy instrument with a 2π field of view for planetary missions," Meas. Sci. Technol. **11**, 375–381 (2000).
[21]Y. Saito, S. Yokota, K. Asamura, T. Tanaka, R. Akiba, M. Fujimoto *et al.*, "Low-energy charged particle measurement by MAP-PACE onboard SELENE," Earth, Planets Space **60**, 375–385 (2008).
[22]B. Su, L. G. Kong, and A. B. Zhang, "Design and simulation of a hot plasma analyzer with a 2π field-of-view and high resolution," J. Astronaut. **40**(5), 604–610 (2019).
[23]H. Rème, J. M. Bosqued, J. A. Sauvaud, A. Cros, J. Dandouras, C. Aoustin *et al.*, "The Cluster Ion Spectrometry (CIS) experiment," Space Sci. Rev. **79**, 303–350 (1997).
[24]A. B. Galvin, L. M. Kistler, M. A. Popecki, C. J. Farrugia, K. D. C. Simunac, L. Ellis *et al.*, "The Plasma and Suprathermal Ion Composition (PLASTIC) investigation on the STEREO Observatories," Space Sci. Rev. **136**, 437–486 (2008).
[25]C. Pollock, T. Moore, A. Jacques, J. Burch, U. Gliese, Y. Saito *et al.*, "Fast plasma investigation for magnetospheric multiscale," Space Sci. Rev. **199**, 331–406 (2016).
[26]J.-A. Sauvaud, A. Fedorov, C. Aoustin, H.-C. Seran, E. Le Comte, M. Petiot *et al.*, "The Mercury Electron Analyzers for the Bepi Colombo mission," Adv. Space Res. **46**, 1139–1148 (2010).
[27]U. Rouzaud, L. Saul, P. Wurz, F. Allegrini, J. Scheer, and D. McComas, "A simple 3D plasma instrument with an electrically adjustable geometric factor for space research," Meas. Sci. Technol. **23**, 025901 (2012).
[28]S. Yokota, Y. Saito, K. Asamura, and T. Mukai, "Development of an ion energy mass spectrometer for application on board three-axis stabilized spacecraft," Rev. Sci. Instrum. **76**, 014501 (2005).
[29]K. Delano, S. A. Fuselier, H. A. Elliott, J. L. Burch, J. Mukherjee, S. Petrinec *et al.*, "The He^{++}/H^{+} density ratio across Earth's subsolar magnetopause and its implications for the presence of a mass-dependent reflection coefficient," J. Geophys. Res.: Space Phys. **124**, 9893–9903, https://doi.org/10.1029/2019ja027182 (2019).
[30]W. L. Teh and S. Zenitani, "Thermodynamic properties of mirror structures in the magnetosheath: MMS observations and double-polytropic MHD simulations," Astrophys. J. **885**, 22 (2019).
[31]F. M. Ipavich, A. B. Galvin, S. E. Lasley, J. A. Paquette, S. Hefti, K.-U. Reiche *et al.*, "Solar wind measurements with SOHO: The CELIAS/MTOF proton monitor," J. Geophys. Res. **103**(A8), 17205–17213, https://doi.org/10.1029/97ja02770 (1998).
[32]W. C. Feldman, J. R. Asbridge, S. J. Bame, and J. T. Gosling, "High-speed solar wind flow parameters at 1 AU," J. Geophys. Res. **81**(28), 5054–5060, https://doi.org/10.1029/ja081i028p05054 (1976).
[33]C. P. Price, D. W. Swift, and L.-C. Lee, "Numerical simulation of nonoscillatory mirror waves at the Earth's magnetosheath," J. Geophys. Res. **91**(A1), 101–112, https://doi.org/10.1029/ja091ia01p00101 (1986).
[34]K. Tsubouchi, T. Nagai, and I. Shinohara, "Stable ring beam of solar wind He^{2+} in the magnetosheath," J. Geophys. Res.: Space Phys. **121**, 1233–1248, https://doi.org/10.1002/2015ja021769 (2016).
[35]X. Li, H. R. Lewis, J. LaBelle, T.-D. Phan, and R. A. Treumann, "Characteristics of the ion pressure tensor in the Earth's magnetosheath," Geophys. Res. Lett. **22**(6), 667–670, https://doi.org/10.1029/95gl00005 (1995).
[36]P. Hill, G. Paschmann, R. A. Treumann, W. Baumjohann, N. Sckopke, and H. Lühr, "Plasma and magnetic field behavior across the magnetosheath near local noon," J. Geophys. Res. **100**(A6), 9575–9583, https://doi.org/10.1029/94ja03194 (1995).
[37]G. L. Kalra and S. Kumar, "Effect of He^{++} ions on the propagation of low-frequency magnetohydrodynamic waves in the magnetosheath," J. Geophys. Res. **111**, A11226, https://doi.org/10.1029/2005ja011453 (2006).
[38]G. Parks, E. Lee, S. Y.Fu, H. E. Kim, Y. Q. Ma, Z. W. Yang *et al.*, "Transport of solar wind H^{+} and He^{++} ions across Earth's bow shock," Astrophys. J. Lett. **825**, L27 (2016).
[39]B. Klecker, "Interplanetary particles and magnetic fields," in *Astronomy, Astrophysics, and Cosmology*, edited by J. E. Trümper (Springer-Verlag, Berlin, Heidelberg, Germany, 2009), pp. 537–559, http://materials.springer.com/lb/docs/sm_lbs_978-3-540-88055-4_33.
[40]R. Schwenn, "The average solar wind in the inner heliosphere: Structures and slow variations," in *Solar Wind Five: Proceedings of the Conference Held in Woodstock, VT*, 1–5 November 1982, edited by M. Neugebauer (NASA Conference Publications, Pasadena, CA, 1983), pp. 489–507, http://hdl.handle.net/2060/19840005037.
[41]J. C. Kasper, M. L. Stevens, A. J. Lazarus, J. T. Steinberg, and K. W. Ogilvie, "Solar wind helium abundance as a function of speed and heliographic latitude: Variation through a solar cycle," Astrophys. J. **660**, 901–910 (2007).
[42]M. R. Aellig, A. J. Lazarus, and J. T. Steinberg, "The solar wind helium abundance: Variation with wind speed and the solar cycle," Geophys. Res. Lett. **28**(14), 2767–2770, https://doi.org/10.1029/2000gl012771 (2001).